Journal of Alloys and Compounds 704 (2017) 776–787

Contents lists available at ScienceDirect

Journal of Alloys and Compounds

journal homepage: http://www.elsevier.com/locate/jalcom

Synthesis, structural characterization and magnetic properties of the series of double perovskites $Ba_{1+x}La_{1-x}MnSbO_6$ with $0.1 \leq x \leq 0.7$

Diana M. Arciniegas Jaimes [a], M. Cecilia Blanco [a], Fernando Pomiro [a], Germán Tirao [b], Vivian M. Nassif [c, d], Gabriel J. Cuello [e], José A. Alonso [f], Raúl E. Carbonio [a, *]

[a] INFIQC (CONICET – Universidad Nacional de Córdoba), Departamento de Fisicoquímica, Facultad de Ciencias Químicas, Universidad Nacional de Córdoba, Haya de la Torre esq, Medina Allende, Ciudad Universitaria, X5000HUA Córdoba, Argentina
[b] IFEG (CONICET), Facultad de Matemáticas, Astronomía y Física, Universidad Nacional de Córdoba, Haya de la Torre esq, Medina Allende, X5000HUA Córdoba, Argentina
[c] Univ. Grenoble Alpes, F-38000 Grenoble, France
[d] CNRS, Inst. NEEL, F-38042 Grenoble, France
[e] Institut Laue Langevin, 71 Av. des Martyrs, CS20156, 38042 Grenoble Cedex 9, France
[f] Instituto de Ciencia de Materiales de Madrid, Sor Juana Inés de la Cruz 3, Cantoblanco, 28049 Madrid, Spain

ARTICLE INFO

Article history:
Received 19 October 2016
Received in revised form
22 December 2016
Accepted 23 December 2016
Available online 26 December 2016

Keywords:
Double perovskites
Crystal structure
Magnetic measurements
Powder neutron diffraction
Order-disorder effects
X-ray emission spectroscopy

ABSTRACT

Double perovskites $Ba_{1+x}La_{1-x}MnSbO_6$ were synthesized by traditional ceramic methods in air as polycrystalline powders. The $0.1 \leq x \leq 0.2$ compounds belong to the I 2/m monoclinic space group, while the perovskites with $x \geq 0.3$ belong to the I 4/m tetragonal space group. The effective presence of mixtures of Mn^{2+}/Mn^{3+} has been well established by X-ray Emission Spectroscopy. $Ba_{1+x}La_{1-x}MnSbO_6$ ($0.1 \leq x \leq 0.5$) oxides display signs of superparamagnetism in the 40–160 K range, which arises from 3D-nanoclusters formed in regions which are rich in $Mn^{2+/3+}$–O–$Mn^{2+/3+}$ superexchange paths originated by the antisite disorder. The analysis of the M vs H hysteresis loops shows that, as x increases, the number of 3D-nanoclusters rises and the number of magnetic ions in the 3D-nanoclusters decreases. The small 3D-nanoclusters cannot sustain magnetic order inside them and this is the reason for the absence of superparamagnetism for $x = 0.6$ and 0.7. The analysis of the M vs H curves also shows the presence of a weak ferromagnetism which is generated by the canting of the spins in the antiferromagnetic matrix. Neutron Powder Diffraction data reveals that there is long range antiferromagnetic ordering below ≈20 K.

1. Introduction

Oxides with the perovskite structure are called “inorganic chameleon” because they exhibit many compositions and properties such as thermal and ionic conductivity, ferromagnetism, semi and super conductivity, optical properties, piezoelectricity, ferroelectricity and oxygen transport, etc. making them suitable for a large variety of applications [1–7]. The discovery of colossal-magnetoresistance (CMR) properties at temperatures significantly above room temperature in the Sr_2FeMoO_6 double perovskite with a high magnetic transition temperature T_C (≈400 K) [4] has renewed the interest on this type of compounds because of their potential importance in magnetotransport and spintronic devices.

The structure of double perovskites, $A_2BB'O_6$, is similar to that of simple perovskites, ABO_3. It can accommodate almost all elements of the periodic table on its cuboctahedral (A) and octahedral (B and B′) sites. Perovskite structure is a three-dimensional arrangement of corner-sharing BO_6 octahedra, with the A-type cations occupying the high coordination sites which usually are alkaline-earth or rare-earth cations; the B and B′ ions are different transition metal cations that can be ordered with a doubling of the normal unit cell. This ordering mostly depends on the size and charge difference among cations and this ordered structure is verified by the appearance of superstructure peaks in the Powder X-ray Diffraction (PXRD) pattern in 2θ around 18° with Cu Kα radiation [8,9]. On the other hand, the ideal structure of perovskites can be described by the Goldschmidt tolerance factor [10] that can be adapted to double

* Corresponding author.
E-mail address: carbonio@fcq.unc.edu.ar (R.E. Carbonio).

http://dx.doi.org/10.1016/j.jallcom.2016.12.308
0925-8388/

perovskites as well. In general, for double perovskites, with mixed A-site, $A_{1+x}A'_{1-x}BB'O_6$ the tolerance factor can be written as:

$$\tau = \frac{\frac{(1-x)*r_{A'} + (1+x)*r_A}{2} + r_{O^{2-}}}{\sqrt{2}\left(\left(\frac{r_B + r_{B'}}{2}\right) + r_{O^{2-}}\right)}$$

where r_A, $r_{A'}$, r_B, $r_{B'}$ and r_O^{2-} are the ionic radii of A, A′, B, B′ and O^{2-} ion. Theoretically, when $\tau = 1$, the perovskite adopts a cubic symmetry (space group *P*m-3m). For $\tau < 1$, the structure is distorted with a symmetry lower than cubic. Thus the tolerance factor is a semi quantitative estimation of how close a perovskite is to the cubic structure; moreover, for a large deviation of τ from 1 the perovskite structure is likely to be unstable.

Three different types of distortions have been identified: *(i)* distortions of the BO_6 octahedra, *(ii)* B cation displacements within the octahedra, and *(iii)* the tilting of the BO_6 octahedra [11,12]. The latter is the most common type of distortion in perovskite structures. The change in the radius of the A site cation causes this tilt in the octahedral sites to optimize the A-O bond distances which implies a change of symmetry in the system. The number of d-electrons of the B-site cation and/or the size of the cations in perovskite materials can contribute to structural distortions and can have effect on their magnetotransport properties [13], therefore, the B cationic ordering degree could change the magnetic and electric properties of the perovskite materials.

Double perovskites of the type AA'BB'O_6 with A = Ca, Sr and Ba; A' = Ln; B = magnetic 3d transition metal ions and B' = 4th and 5th rows transition metal ions or diamagnetic like Sb^{5+} [14–16], and others with doping in the A or A′ cation positions, have already been studied by different authors [13,17–21]. Most of them are highly ordered double perovskites, with predominant antiferromagnetic interactions and/or magnetic frustration as a consequence of different competing magnetic interactions in the materials. This may be due to the different kinds of structural distortions and order/disorder between B and B′ cations.

In a previous work, the undoped $BaLaMnSbO_6$ (with 100% Mn as 2+) was synthesized and its structural and magnetic properties were analyzed [22]. It belonged to the I 2/m monoclinic space group and presented an antiferromagnetic transition at $T_N \approx 14$ K. Also displayed superparamagnetism (SPM) in the 40–160 K range ($T_C \approx 160$ K). The effective presence of Mn^{2+} was well established by X-ray emission spectroscopy (XES) and there was no evidence of Mn^{3+}. Also, Chandrahas Bharti et al. [23] reported the synthesis and electrical properties of a tetragonal $BaLaMnSbO_6$ double perovskites.

In this work, we have successfully synthesized the new B-site ordered double perovskite oxides (DPOs) $Ba_{1+x}La_{1-x}MnSbO_6$ ($0.1 \leq x \leq 0.7$) containing Mn^{2+}/Mn^{3+} and Sb^{5+} as B and B′ ions, respectively. As Ba^{2+} content increases, Mn^{2+} should be oxidized to Mn^{3+} and the difference of charge between B and B′ decreases. This is interesting because this could have an influence on the disorder and consequently on the measured properties. We present their synthesis, structural characterization using Powder X-ray Diffraction (PXRD) and Powder Neutron Diffraction (PND), magnetic characterization using Magnetization (M) vs. Temperature (T) and M vs. Magnetic field (H) measurements, and Mn ion oxidation state determination from XES.

2. Materials and methods

2.1. Sample preparation

Polycrystalline samples of $Ba_{1+x}La_{1-x}MnSbO_6$ ($0.1 \leq x \leq 0.7$) were prepared through standard solid-state reactions from stoichiometric amounts of $BaCO_3$, La_2O_3, MnO, and Sb_2O_3, all of them in analytical grade. First of all, La_2O_3 was dried, previous to use at 900 °C in air during 16 h. The reagents were mixed in agate mortar, pelletized and heat treated in alumina boats under air atmosphere. Due to the low melting point of Sb_2O_3, the mixtures were first heated at 780 °C for 12 h, then at 900 °C for 9 h and finally at different temperatures between 1315°C–1440 °C during 24 h, depending on each sample. All heating and cooling rates were 3 °C/min. Attempts to prepare the compounds with $x > 0.7$ were fruitless.

2.2. Powder X-ray and Neutron diffraction and Rietveld analysis

PXRD patterns were measured at room temperature on a PANanalitycal X'Pert Pro diffractometer (40 kV, 40 mA) in Bragg–-Brentano geometry with Cu Kα radiation in the range 10–100° with step size of 0.02° and with a step counting time of 10 s. PND patterns were collected in the D2B powder diffractometer [24] ($\lambda = 1.594$ Å) at 300 K and 4 K for all samples, and D1B powder diffractometer [25] ($\lambda = 1.28$ Å) was used to obtain information for $x = 0.2$ sample at different temperatures; all these measurements were performed at the Institute Laue-Langevin (ILL), Grenoble, France. The measurements were performed in the angular range from 0° to 159.95° with steps of 0.05° on D2B and 0.77°–128.77° with a step of 0.1°on D1B. Structure refinement of the PXRD and PND patterns were performed by the Rietveld method using the FullProf program [26,27]. The pseudo-Voigt peak-shape function was used for PXRD and a Thompson-Cox-Hastings pseudo-Voigt convoluted with axial divergence asymmetry shape function was used for PND. The refined parameters were: background, scale factor, zero shift, cell parameters, atomic positions, occupancies, isotropic atomic displacement parameters, as well as the usual profile parameters describing the peak shape functions.

2.3. X-ray emission spectroscopy

High-resolution Kβ XES spectra of $Ba_{1+x}La_{1-x}MnSbO_6$ ($0.1 \leq x \leq 0.7$), simple manganese oxides MnO, Mn_2O_3, MnO_2 and the undoped $BaLaMnSbO_6$ ($x = 0$), with known oxidation states were measured using a non-conventional spectrometer [28] based on quasi-backdiffraction geometry.

The whole spectrometer (sample holder, analyser and detector) is enclosed in an evacuated chamber, in order to avoid X-ray attenuation and scattering from air. The measurements were performed at conventional 45°-45° geometry. The whole spectrum from a cobalt-target X-ray conventional tube, operated at 40 mA and 37 kV, was used as irradiation source [29]. The high resolution Kβ emission spectra were recorded by scanning, in steps of about 0.3 eV around the $K\beta_{1,3}$ main line, the analyser and the detector synchronously. With a spot size of 1.2 mm^2, the measured counting rate, as example for $Ba_{1.4}La_{0.6}MnSbO_6$ and MnO at the $K\beta_{1,3}$ line was around 80 cps and 1000 cps, respectively, and the signal-to-background ratio was better than 70. The resolution of this spectrometer was determined to be 0.8 eV for the Mn-$K\beta_{1,3}$ line (for calculation details see Ref. [28]), and the energy scale was calibrated using the value of the $K\beta_{1,3}$ line of Mn^0 given by Bearden [30] ($EK\beta_{1,3} = 6490.45$ eV).

To calculate the spectral parameters, the spectra were first normalized to a constant value for the maximum of $K\beta_{1,3}$ line. Then three Voigt function, representing the Kβ′, $K\beta_x$ and $K\beta_{1,3}$ peaks, and the EMG (Exponentially Modified Gaussian) function, to include KMM radiative Auger effect (RAE) [31–33], were fitted in order to reproduce the peaks features, and a linear background was subtracted. The energy position of the RAE peak was determined from the atomic energy of the $M_{4,5}$ level [34]. The experimental

resolution was characterized by the Gaussian width. The experimental errors of the studied spectral parameters were determined from the fitting errors.

The main Kβ lines originate in the 3p → 1s transition of the central metallic atom, while satellite structures can provide information on the oxidation state, type of ligand and metal-ligand binding length [35]. For Mn-compounds, with 3d unpaired electrons, the main Kβ region splits into multiplets spread over a region of about 15eV, being mainly composed of the strong $K\beta_{1,3}$ line and a less intense Kβ′ and $K\beta_x$ satellite lines at lower energies. These structures may be explained by ligand field multiplet model, where Kβ′ line is due to the 3p3d exchange interaction and $K\beta_x$ line due to spin flip of the 3d electron [36]. Besides the radiative events, the RAE is a process competitive to emission of the diagram line, in which the inner-shell hole is filled by a transition of an electron from an outer shell electron [37]. The $KM_{2,3}M_{4,5}$ transitions correspond to K-M2,3 transitions that could be associated to the Kβ1,3 line with emission of an M4,5 electron. This phenomenon is observed as a peak located at the low-energy side of Kβ1,3 main peak producing an asymmetric peak shape. For first row transition atoms, variations in the KM2,3M4,5 RAE intensity is related with the oxidation state, since this line is related to 3d electrons.

2.4. Magnetic measurements

The magnetic measurements were performed using a commercial MPMS-5S superconducting quantum interference device magnetometer (SQUID), on powdered samples, from 4 to 350 K at 1000 Oe in ZFC-FC modes and isothermal magnetization loops were performed at 5 and 300 K.

3. Results and discussion

3.1. Crystallographic and magnetic structure

The PXRD patterns for $Ba_{1+x}La_{1-x}MnSbO_6$ ($0.1 \leq x \leq 0.7$) samples collected at RT are shown in Fig. 1a and b. The patterns display a double perovskite-like phase with a good crystallinity and no impurities. The crystallographic characterization was performed by using PND data. Initially, the structures were refined in the monoclinic I 2/m space group, taking as starting structural model the one of undoped $BaLaMnSbO_6$ [22]. As it can be seen in Fig. 1c and d, the PXRD patterns show notable changes in the peak's shape at higher angles values along the series. Also, measurements of PND were made and analyzed for all samples. When all the PXRD and PND patterns were first refined with the monoclinic space group, the *a* and *b* cell parameters were more similar among them and *β* tends to 90° when x increases. Previous studies have shown that in doped double perovskites, the symmetry gains when increasing the average size of the A-site cation (r_A) as is the case of $La_{2-x}Sr_xCoIrO_6$ [38] and $A_{2-x}Sr_xNiWO_6$ with A = Ca or Ba, double perovskites [13]. For this reason, a set of space groups of higher symmetry than I 2/m were explored, and the best results were obtained with the tetragonal I 4/m space group. The same space group was used previously to refine the $BaLaCoSbO_6$ double perovskite [22]. Antisite disorder was determined from the refinement of PND data measured at room temperature, by allowing the occupancies of Mn and Sb ions in their respective positions to be varied. The best results for the Rietveld refinement of the RT PND patterns for x = 0.2 and x = 0.7 are shown in Fig. 2a and b, showing that $Ba_{1+x}La_{1-x}MnSbO_6$ belongs to the monoclinic space group I 2/m for $x \leq 0.2$ and tetragonal space group I 4/m for $x \geq 0.3$.

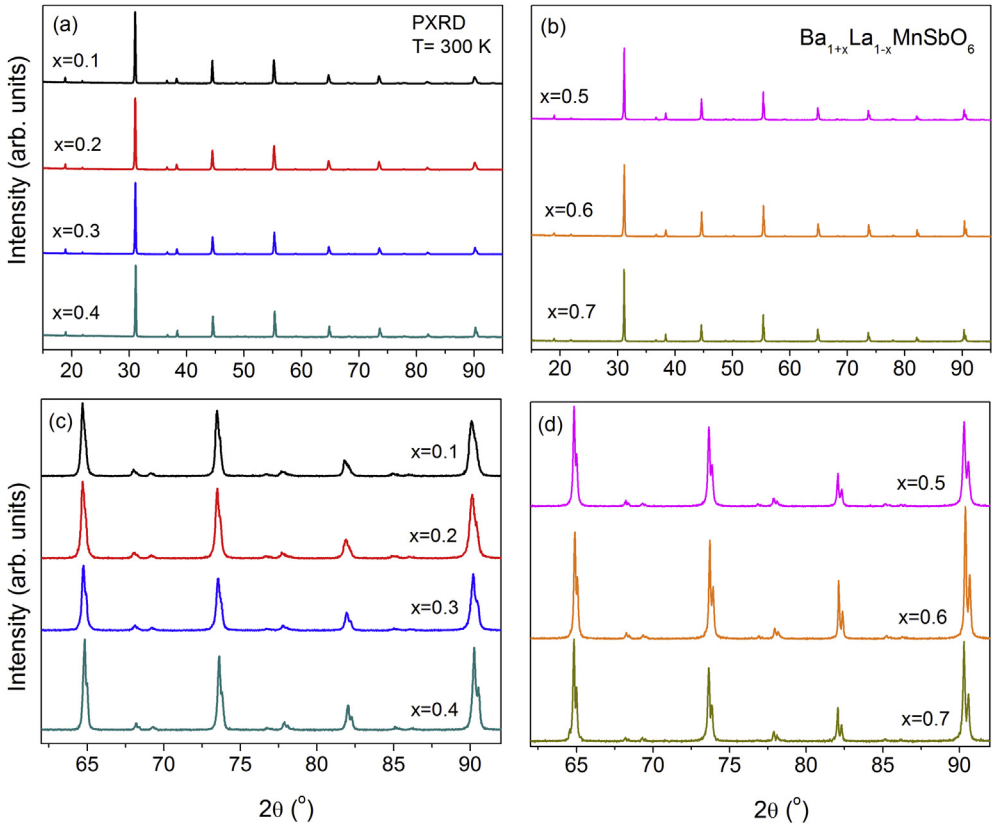

Fig. 1. Room temperature PXRD patterns for $Ba_{1+x}La_{1-x}MnSbO_6$ samples **a)** $0.1 \leq x \leq 0.4$ and **b)** $0.5 \leq x \leq 0.7$. Zoom view for the higher angles region for **c)** $0.1 \leq x \leq 0.4$ and **d)** $0.5 \leq x \leq 0.7$.

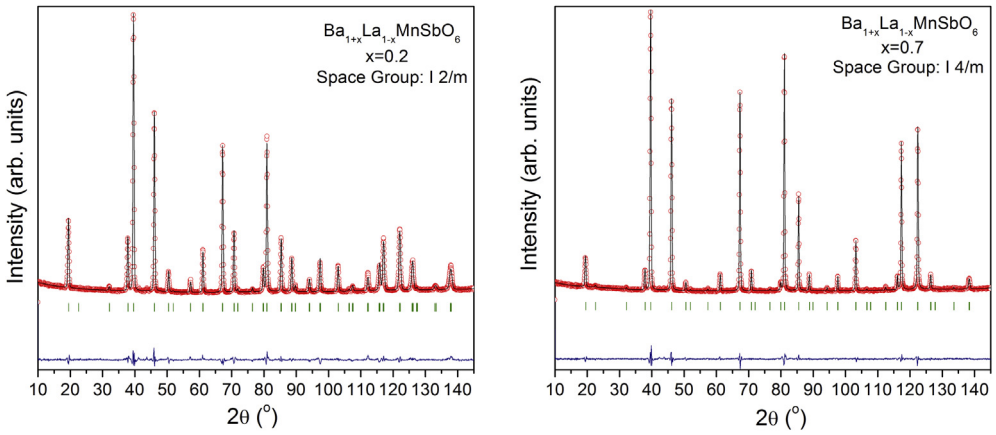

Fig. 2. Observed (red dots), calculated (black full line), Bragg reflections (vertical green bars) and difference (blue bottom line) for PND patterns at 300 K after the refinement of the crystal structure of $Ba_{1+x}La_{1-x}MnSbO_6$ for **a)** x = 0.2 and **b)** x = 0.7. (For interpretation of the references to colour in this figure legend, the reader is referred to the web version of this article.)

PND is an essential technique when two ions have similar X-ray scattering factors because of their proximity in the periodic table. They can have different neutron scattering lengths and PND data allow a better refinement of occupancies and thus, anti-site disorder. For these compounds the neutron scattering lengths are 5.07 fm for Ba, 8.24 fm for La, −3.73 fm for Mn and 5.57 fm for Sb [39]. These are sufficiently contrasting to refine occupancies of the A, A′, B and B′ sites respectively.

Unit-cell parameters *a*, *b*, *c*, *β* and cell volume as a function of x at 300 K determined by PND Rietveld refinement are shown in Table 1. The volume presents a non-monotonic behaviour and it is likely due to the presence of two different phenomena in the system: *i)* the doping with a bigger <A> cation tends to expand the cell and *ii)* the concomitant increase in oxidation state from Mn^{2+} to Mn^{3+} produces a reduction of the average radius of the Mn ions as has been observed previously in the related series $La_{2-x}Sr_xCoTiO_6$ in which case Co^{2+} is oxidized to Co^{3+} and their volume decrease even it is being doped with a bigger A (Sr^{2+}) [20,40]. These two phenomena are present in $Ba_{1+x}La_{1-x}MnSbO_6$ and depending on the particular sample, one effect prevails over the other. For x = 0–0.2 and 0.6–0.7, the volume growths, so, in these samples, the volume effect is due to <A> cation size; for x = 0.3–0.5, the volume diminish, indicating that oxidation of Mn^{2+} is the main mechanism for the volume change.

When the PND data measured at 4 K for $Ba_{1+x}La_{1-x}MnSbO_6$ were analyzed, the same I 2/m symmetry for 0.1 ≤ x ≤ 0.2 and I 4/m symmetry for x ≥ 0.3 were found; only a small contraction of the unit cell was detected as can be seen in Table 1. The structural parameters obtained by Rietveld refinement from PND data at 300 K and 4 K are shown in Table 2, where we observe a very low B cation anti-site disorder (ASD) that increases with x. This is because B-cation ordering is favoured mainly by a charge difference between B and B′ cations, so the charge difference between Mn and Sb begins to be smaller when Mn^{3+} fraction increases [8].

Oxygen vacancies in a low quantity were found for x ≥ 0.3, which are lower than 1%. Also, the Wyckoff sites, atomic positions and temperature factors (B_{iso}) are informed in Table 2.

For 300 K data, Fig. 3a shows that average ⟨B′-O⟩ (B′ site mainly occupied by Sb) distance is shorter than average ⟨B-O⟩ (B site mainly occupied by Mn) distance because Sb^{5+} cation has a smaller ionic radius. Clearly, the ⟨B′-O⟩ distances rise slightly when x increases, and this is likely due to the oxidation of Mn^{2+} to Mn^{3+} since Mn^{3+} has an ionic radii closer to Sb^{5+} (Mn^{2+}(HS) = 0.97 Å; Mn^{3+} (HS) = 0.785 Å; Sb^{5+} = 0.74 Å) [41] and it accommodates preferentially in Sb^{5+} octahedral sites (r^{3+}_{Mn} is ≈ 1.06 r^{5+}_{Sb}).

$Ba_{1+x}La_{1-x}MnSbO_6$ oxides have two different tilt systems, according to Glazer's notation. For I 2/m monoclinic double perovskites belongs to $a^-a^-c^0$ tilt system and $a^0a^0c^-$ for I4/m tetragonal double perovskites. The tilt angles can be estimated as δ = (180-θ)/2, where θ is the angle B-O-B′ shown in Fig. 3b for each sample. The tilt angles are shown in Table 3 for all samples and it can be seen that for large values of x, the tilt angles begin to be lower and smaller than 10°, suggesting the gain of symmetry. This is related to the tolerance factor (*τ*) whose values are ≈ 0.97 and ≈ 1.02 for

Table 1
Refined unit-cell parameters and discrepancy factors after the Rietveld refinement from PND data at 300 K and 4 K for $Ba_{1+x}La_{1-x}MnSbO_6$.

x	Space group	T (K)	a(Å)	b(Å)	c(Å)	β(°)	V(Å3)	χ^2	R_{wp} (%)	R_p (%)	R_{Bragg} (%)
0.1	I 2/m	300	5.7592(2)	5.7625(1)	8.1457(2)	90.175(2)	270.34(1)	5.17	10.2	11.9	4
		4	5.7495(1)	5.7530(1)	8.1314(2)	90.200(2)	268.96(1)	3.54	10.6	11.9	3.93
0.2	I 2/m	300	5.7639(3)	5.7591(3)	8.1446(2)	90.087(4)	270.36(2)	3.72	9.53	11.2	3.26
		4	5.7537(2)	5.7495(2)	8.1300(2)	90.111(4)	268.95(1)	3.64	9.52	10.5	3.14
0.3	I 4/m	300	5.7570(1)	5.7570(1)	8.1461(3)	90	269.99(1)	2.63	9.86	12.7	3.42
		4	5.7460(1)	5.7460(1)	8.1325(2)	90	268.51(1)	3.07	10.6	13.3	3.55
0.4	I 4/m	300	5.7545(1)	5.7545(1)	8.1423(3)	90	269.63(1)	3.64	9.19	11	3.02
		4	5.7436(1)	5.7436(1)	8.1283(2)	90	268.14(1)	3.86	9.99	11.8	3.47
0.5	I 4/m	300	5.7513(1)	5.7513(1)	8.1383(2)	90	269.20(1)	2.97	7.75	9.44	2.01
		4	5.7402(1)	5.7402(1)	8.1230(1)	90	267.65(1)	2.98	8.26	9.86	2.60
0.6	I 4/m	300	5.7488(4)	5.7488(4)	8.1242(1)	90	268.50(1)	3.47	8.11	9.55	1.82
		4	5.7375(1)	5.7375(1)	8.1088(1)	90	266.94(1)	2.73	8.83	10.6	2.21
0.7	I 4/m	300	5.7530(1)	5.7530(1)	8.1299(1)	90	269.07(1)	3.11	7.8	9.42	2.05
		4	5.7388(1)	5.7388(1)	8.1226(1)	90	267.50(1)	2.24	8.95	10.9	1.84

Table 2
Positional, thermal parameters and occupancies for $Ba_{1+x}La_{1-x}MnSbO_6$ after Rietveld refinement from PND data at 300 K and 4 K. The Occ. values are normalized to 1 for sites 1 and 2.

x	Ion	Wyckoff site	T(K)	x	y	z	B_{iso}	Occ
0.1	Ba/La	4i	300	0.4964(1)	0.0000	0.2511(9)	0.96(5)	1.1(4)/0.9(4)
S.G:			4	0.4951(1)	0.0000	0.2506(8)	0.58(4)	
I 2/m	Mn/Sb(1)	2d	300	0.0000	0.0000	0.5000	1.66(3)	0.976(5)/0.024(5)
			4	0.0000	0.0000	0.5000	1.55(3)	
	Mn/Sb(2)	2a	300	0.0000	0.0000	0.0000	0.99(1)	0.05(8)/0.94(8)
			4	0.0000	0.0000	0.0000	0.89(1)	
	O1	4i	300	−0.0366(9)	0.0000	0.2444(6)	0.56(7)	2.00(1)
			4	−0.0397(8)	0.0000	0.2442(6)	0.31(7)	
	O2	8j	300	0.2295(9)	0.2442(1)	0.0308(4)	2.23(9)	4.00(3)
			4	0.2283(8)	0.2462(1)	0.0316(4)	1.91(9)	
0.2	Ba/La	4i	300	0.5045(4)	0.0000	0.2516(4)	0.98(6)	1.2 (4)/0.8(4)
S.G:			4	0.5029(3)	0.0000	0.2517(3)	0.59(5)	
I 2/m	Mn/Sb(1)	2d	300	0.0000	0.0000	0.5000	2.13(3)	0.968(4)/0.032(4)
			4	0.0000	0.0000	0.5000	1.99(3)	
	Mn/Sb(2)	2a	300	0.0000	0.0000	0.0000	1.28(1)	0.040(6)/0.960(6)
			4	0.0000	0.0000	0.0000	1.17(2)	
	O1	4i	300	−0.0309(3)	0.0000	0.2413(3)	0.50(7)	2.00(1)
			4	−0.0335(2)	0.0000	0.2411(2)	0.26(7)	
	O2	8j	300	0.2363(3)	0.2427(4)	0.0273(8)	2.26(9)	4.00(1)
			4	0.2368(2)	0.2430(2)	0.0283(1)	1.96(9)	
0.3	Ba/La	4d	300	0.0000	0.5000	0.2500	0.77(4)	1.3(2)/0.7(2)
S.G:			4	0.0000	0.5000	0.2500	0.41(4)	
I 4/m	Mn/Sb(1)	2a	300	0.0000	0.0000	0.0000	1.65(2)	0.976(2)/0.024(2)
			4	0.0000	0.0000	0.0000	1.39(2)	
	Mn/Sb(2)	2b	300	0.0000	0.0000	0.5000	1.09(2)	0.024(3)/0.976(3)
			4	0.0000	0.0000	0.5000	0.96(1)	
	O1	4e	300	0.0000	0.0000	0.2572(2)	3.56(2)	1.95(1)
			4	0.0000	0.0000	0.2554(2)	3.43(1)	
	O2	8h	300	0.2794(1)	0.2377(9)	0.0000	1.18(5)	4.00(1)
			4	0.2810(1)	0.2355(8)	0.0000	0.90(5)	
0.4	Ba/La	4d	300	0.0000	0.5000	0.2500	0.74(5)	1.4(2)/0.6(2)
S.G:			4	0.0000	0.5000	0.2500	0.38(4)	
I 4/m	Mn/Sb(1)	2a	300	0.0000	0.0000	0.0000	1.60(2)	0.952(2)/0.048(2)
			4	0.0000	0.0000	0.0000	1.45(2)	
	Mn/Sb(2)	2b	300	0.0000	0.0000	0.5000	1.01(1)	0.048(3)/0.952(3)
			4	0.0000	0.0000	0.5000	0.91(1)	
	O1	4e	300	0.0000	0.0000	0.2568(2)	2.88(1)	1.98(1)
			4	0.0000	0.0000	0.2569(2)	2.54(1)	
	O2	8h	300	0.2732(1)	0.2417(9)	0.0000	1.20(5)	4.00(2)
			4	0.2746(1)	0.2396(8)	0.0000	0.94(5)	
0.5	Ba/La	4d	300	0.0000	0.5000	0.2500	0.66(1)	1.5(2)/0.5(2)
S.G:			4	0.0000	0.5000	0.2500	0.37(3)	
I 4/m	Mn/Sb(1)	2a	300	0.0000	0.0000	0.0000	1.11(1)	0.920(2)/0.080(2)
			4	0.0000	0.0000	0.0000	0.97(1)	
	Mn/Sb(2)	2b	300	0.0000	0.0000	0.5000	0.67(8)	0.080(3)/0.920(3)
			4	0.0000	0.0000	0.5000	0.54(7)	
	O1	4e	300	0.0000	0.0000	0.2568(1)	2.06(1)	1.96(1)
			4	0.0000	0.0000	0.2572(1)	1.95(1)	
	O2	8h	300	0.266(1)	0.2454(9)	0.0000	1.38(7)	4.00(2)
			4	0.2662(8)	0.2440(7)	0.0000	1.08(6)	
0.6	Ba/La	4d	300	0.0000	0.5000	0.2500	0.62(4)	1.6(2)/0.4(2)
S.G:			4	0.0000	0.5000	0.2500	0.34(4)	
I 4/m	Mn/Sb(1)	2a	300	0.0000	0.0000	0.0000	0.73(1)	0.872(3)/0.128(2)
			4	0.0000	0.0000	0.0000	0.63(1)	
	Mn/Sb(2)	2b	300	0.0000	0.0000	0.5000	0.58(8)	0.120(3)/0.880(3)
			4	0.0000	0.0000	0.5000	0.39(8)	
	O1	4e	300	0.0000	0.0000	0.2544(9)	1.58(3)	1.97(1)
			4	0.0000	0.0000	0.2542(9)	1.40(2)	
	O2	8h	300	0.2616(1)	0.2479(1)	0.0000	1.41(1)	4.00(2)
			4	0.2610(1)	0.2479(1)	0.0000	1.06(9)	
0.7	Ba/La	4d	300	0.0000	0.5000	0.2500	0.60(3)	1.7(2)/0.3(2)
S.G:			4	0.0000	0.5000	0.2500	0.28(3)	
I 4/m	Mn/Sb(1)	2a	300	0.0000	0.0000	0.0000	1.29(2)	0.840(1)/0.160(1)
			4	0.0000	0.0000	0.0000	0.0000	
	Mn/Sb(2)	2b	300	0.0000	0.0000	0.5000	0.59(9)	0.152(2)/0.848(2)
			4	0.0000	0.0000	0.5000	0.33(9)	
	O1	4e	300	0.0000	0.0000	0.2540(1)	1.40(3)	1.96(1)
			4	0.0000	0.0000	0.2549(8)	1.09(3)	
	O2	8h	300	0.2606(1)	0.2468(1)	0.0000	1.32(1)	4.00(1)
			4	0.2587(1)	0.2475(1)	0.0000	1.02(7)	

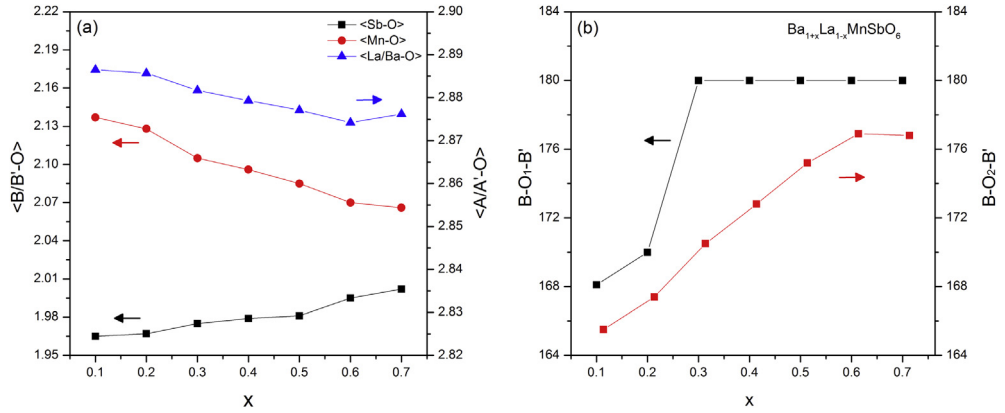

Fig. 3. Average bond distances and angles for $Ba_{1+x}La_{1-x}MnSbO_6$ after Rietveld refinement of PND data at 300 K **a)** Main average distances as functions of x and **b)** B-O-B′ angles as functions of x.

Table 3
Tilt angles (°) for [100], [010] and [001] pseudo-cubic directions of the perovskite obtained from refinement of 300 K PND data.

x	δ	δ	δ
0.1	5.95	7.25	0
0.2	5.00	6.30	0
0.3	0	0	4.75
0.4	0	0	3.60
0.5	0	0	2.40
0.6	0	0	1.55
0.7	0	0	1.60

$x = 0.1$ and $x = 0.7$ respectively, and their values linearly increase with x.

From PND data taken at 4 K, $Ba_{1+x}La_{1-x}MnSbO_6$ presents new peaks at low angles in 2θ from $x = 0.1$ to $x = 0.5$, and these new peaks are very low for $x = 0.6$ and $x = 0.7$. Fig. 4a–c, show the low angle regions for $x = 0.2$, 0.4 and 0.7. It is evident that the magnetic long range order (LRO) starts to vanish with increasing x values. Rietveld refinements of PND data at 4 K were done with both crystalline and magnetic structures using an antiferromagnetic unit-cell with propagation vector $k = 0$ and they are illustrated for $x = 0.2$ and $x = 0.7$ (I 2/m and I 4/m space groups respectively) in Fig. 5a and b.

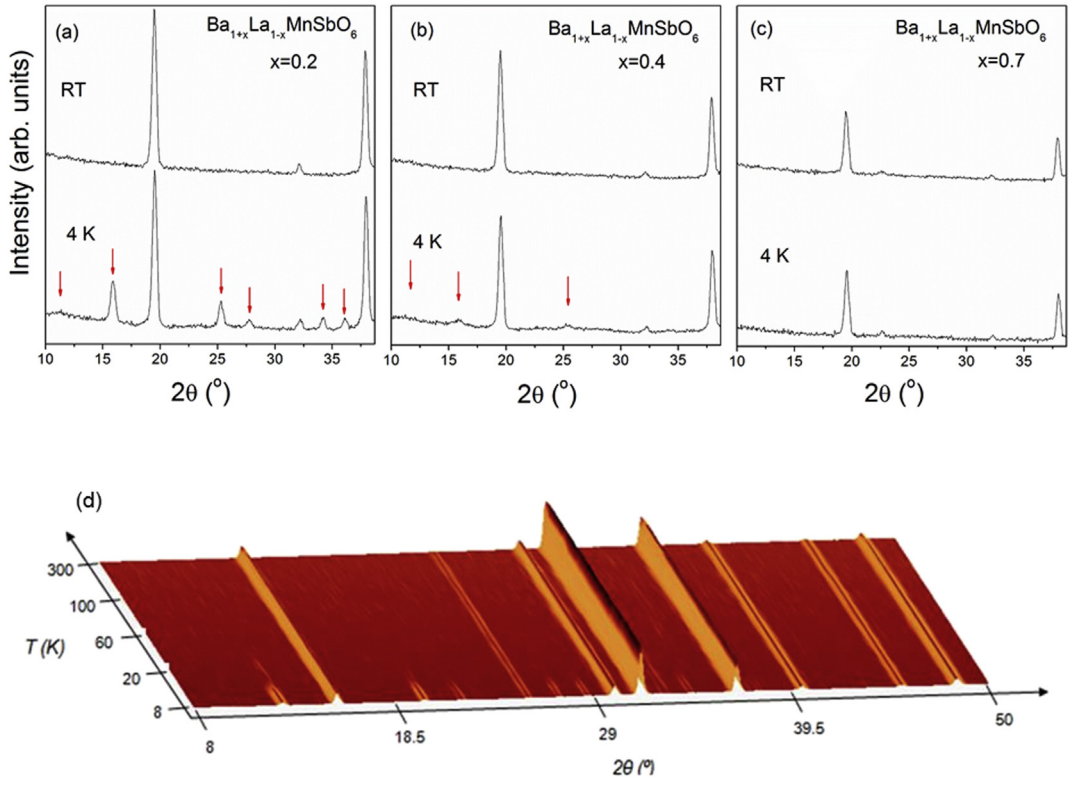

Fig. 4. Upper panel: Comparison between PND data at 4 K and 300 K with λ = 1.594 Å on D2B instrument for **a)** $x = 0.2$, **b)** $x = 0.4$ and **c)** $x = 0.7$ (arrows corresponds to long range magnetic order reflections). **Lower panel**: Thermal evolution of the PND pattern for **d)** $Ba_{1.2}La_{0.8}MnSbO_6$ with λ = 1.28 Å on D1B instrument.

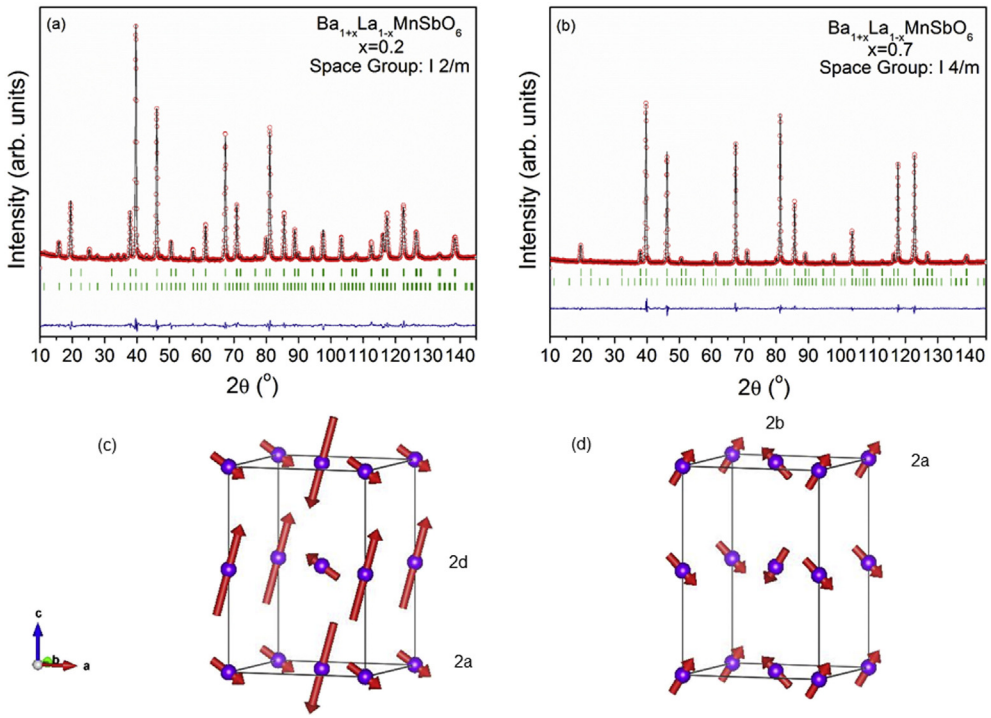

Fig. 5. Upper panel: PND data refinement including crystallographic and magnetic phases at 4 K for **a)** $Ba_{1.2}La_{0.8}MnSbO_6$ and **b)** $Ba_{1.7}La_{0.3}MnSbO_6$. **Lower panel**: Magnetic cell for 4 K PND data, Ba^{2+}, La^{3+} and O^{2-} ions are omitted for simplicity. The arrows represent the effective magnetic moments for **c)** $Ba_{1.2}La_{0.8}MnSbO_6$ of 2d (mainly Mn^{2+}) and 2a (mainly Sb^{5+}) octahedral sites and **d)** $Ba_{1.7}La_{0.3}MnSbO_6$ of 2a (mainly Mn^{2+}) and 2b (mainly Sb^{5+}) octahedral sites.

The structural parameters, main bond distances and angles at 4 K are shown in Table 2, displaying a similar trend than those at 300 K. Two magnetic moments were refined in the magnetic cell corresponding to B and B' (Wyckoff sites 2*d* and 2*a* for I 2/m samples; 2*a* and 2*b* for I 4/m). Magnetic moments corresponding to the site mainly occupied with Sb were found to have a lower value and even negligible in the case of $BaLaMnSbO_6$ [22]. The refined magnetic cells are shown in Fig. 5 for x = 0.2 and x = 0.7, and the corresponding refined magnetic moments are displayed in Table 4. The refined ordered magnetic moments are always lower than the theoretical values calculated for Mn^{2+}/Mn^{3+} fractions for each sample. This great difference between experimental and theoretical values may be due to a magnetic frustration in this perovskite system.

PND patterns for x = 0.2 were collected in the temperature range T = 8–300 K on D1B powder diffractometer [25] with the aim to achieve information about the magnetic moments. The sequential PND patterns are shown in Fig. 4d. The study of the thermal evolution for the PND diagrams shows that the magnetic structure remains stable throughout the temperature range below the ordering temperature. PND data contain extra peaks at low Bragg angles; this is a proof of a LRO magnetic structure below ≈18 K and it is in agreement with magnetic measurements shown below.

Table 4
Magnetic moments of crystallographic sites obtained from refinement of 4 K PND data.

x	Magnetic moments (μ_B)	
	Site (Mn/Sb)1	Site (Mn/Sb)2
0.1	3.09 (3)	0.2 (1)
0.2	2.72 (3)	0.2 (1)
0.3	2.09 (4)	0.3 (2)
0.4	1.20 (5)	0.2 (1)
0.5	0.6 (2)	0.03 (8)
0.6	0.3 (5)	0.4 (5)
0.7	0.3 (5)	0.3 (7)

3.2. X-ray emission spectroscopy

Fig. 6a shows the experimental spectrum and the fitting obtained for $Ba_{1+x}La_{1-x}MnSbO_6$ for x = 0.7. We observe a slight shoulder on the low energy side of the main line (contribution of the $K\beta_x$ satellite line) and the contributions of RAE $KM_{2,3}M_{4,5}$ peak ($K-M_{2,3}$ transition with an emission of a $M_{4,5}$ electron), showing a very good fitting with the proposed model. For this reason, in order to quantify the oxidation state, it is necessary to select those spectral parameters that vary linearly with the oxidation state of the standard samples. We decided to use the intensity of RAE $KM_{2,3}M_{4,5}$ relative to the total area of Kβ region (hereafter IRAE) and the Kβ′ intensity relative to the total intensity of Kβ region (IKβ′). Using theses parameters, we determined the oxidation states of Mn for $Ba_{1+x}La_{1-x}MnSbO_6$ samples from the parameters of the linear fit of Mn simple oxides data, as shown in Fig. 6b and c. The calculated samples oxidation states values and corresponding uncertainties, determined by error propagation, are presented as an inset in the corresponding figures.

The increase in the IRAE with oxidation state, as shown in Fig. 6b, can be qualitative explained, regardless the multiplet contribution [42], by the change in the screening effect in the 3d shell. When the oxidation state increases, the number of electrons in the 3d shell declines so its screening effect is reduced, then, the 3d electrons became more localized. The localized electrons are more subject to the sudden change in the atomic potential than the delocalized electrons; hence the localized electrons are more easily shaken off from the atom and the probability of corresponding RAE process rises [33]. The Kβ′ feature presents a broad peak at the low

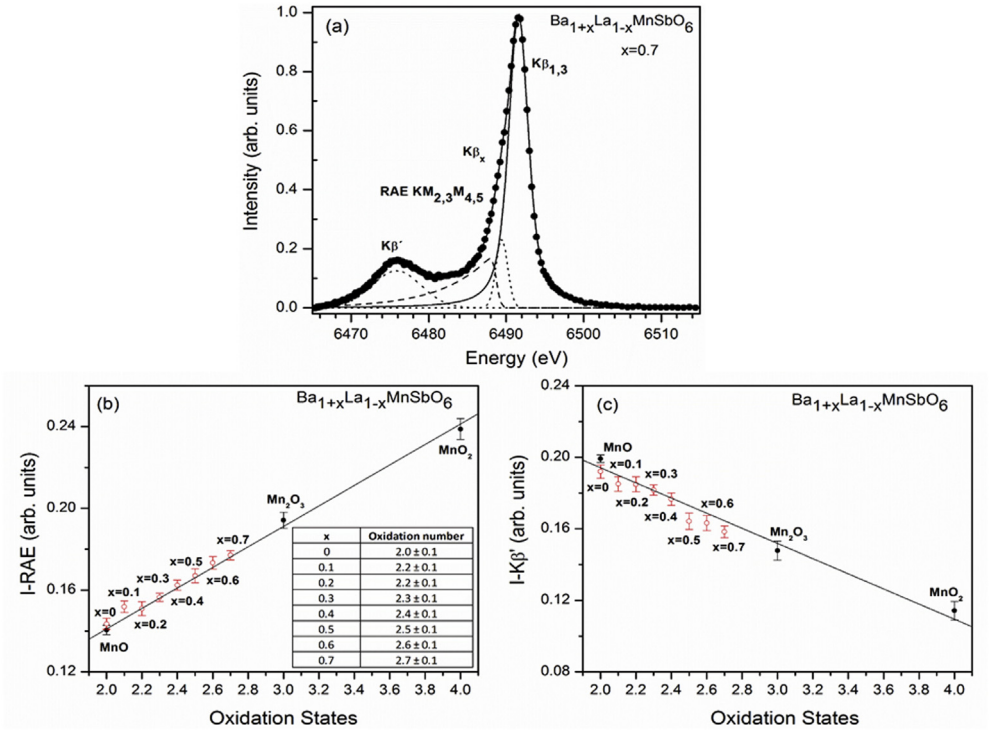

Fig. 6. **a)** Mn-Kβ emission spectrum of $Ba_{1.7}La_{0.3}MnSbO_6$. (Dots): Experimental data. (Continuous and dashed lines): Fitted curve and the corresponding contributions of individual Voigt (Kβ′, $K\beta_x$ and $K\beta_{1,3}$ peaks) and EMG ($KM_{2,3}M_{4,5}$ RAE transition) functions. **b**) Intensity of RAE $KM_{2,3}M_{4,5}$ peak relative to the total area of Kβ region as a function of Mn oxidation states (inset table: oxidation state of Mn obtained from calibration line) and **c)** Intensity of the Kβ′ line relative to the total intensity of the main Kβ region, as a function of oxidation states.

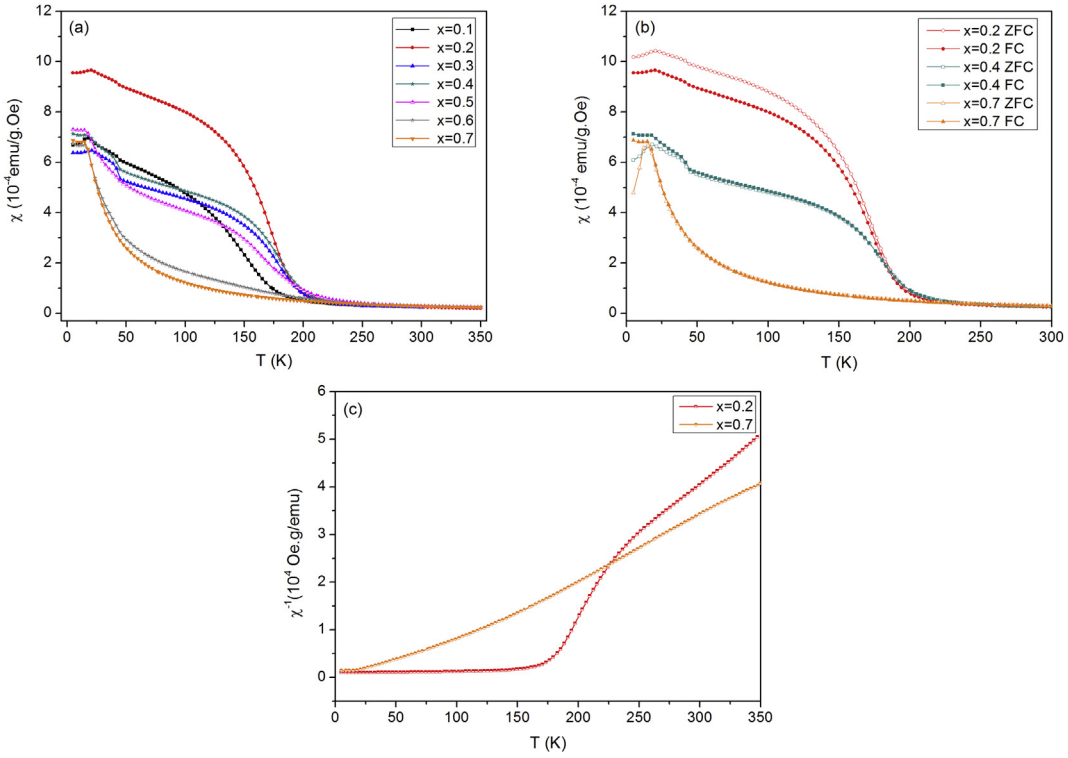

Fig. 7. **a)** χ vs. T at 1000 Oe (field-cooled), **b)** χ vs T at 1000 Oe (Field- Cooled and Zero Field Cooled curves) for x = 0.2, x = 0.4 and x = 0.7 and **c)** χ^{-1} Vs T at 1000 Oe for field-cooled for $Ba_{1.2}La_{0.8}MnSbO_6$ and $Ba_{1.7}La_{0.3}MnSbO_6$.

Table 5
Magnetic parameters obtained according to Curie–Weiss law fitting of FC data in the paramagnetic region. Ferromagnetic transition temperature: Tc; Neel temperature: T_N; Weiss temperature: θ; Experimental paramagnetic effective moment and theoretical one: μ_{eff} and $\mu_{eff\ theo}$.

x	T_N (K)	T_C (K)	θ_W (K)	μ_{eff} (μ_B/Mn^{2+} and Mn^{3+})	$\mu_{eff\ theo}$ (μ_B/Mn^{2+} and Mn^{3+})
0.1	18.0	150	35.7	5.39	5.80
0.2	20.3	173	98.7	4.66	5.70
0.3	20.5	178	78.2	4.82	5.62
0.4	17.6	180	93.6	4.86	5.50
0.5	15.0	165	54.8	5.55	5.40
0.6	14.8	–	77.3	5.39	5.30
0.7	14.6	–	60.8	5.58	5.20

energy side of the main $K\beta_{1,3}$ line which becomes more noticeable for low oxidation states. The energy of the Kβ′ satellite line relative to the main $K\beta_{1,3}$ line decreases linearly with the oxidation state in agreement with results reported by other authors [33,35,43–45]. The intensity of the Kβ′ line (I-Kβ′) relative to the total intensity of the main Kβ region (including the Kβ′ and $K\beta_{1,3}$ lines, whose intensity per Mn must be chemically invariant [35], decreases as the oxidation state increases, as shown in Fig. 6c.

From this analysis we obtain the oxidation states of Mn for all the samples, which are in good agreement with the theoretical oxidation states. It can be seen in the inset table in Fig. 6b, that the oxidation state increases gradually with x values, which is an indication of the presence of mixed oxidation states Mn^{2+}/Mn^{3+}.

3.3. Magnetic characterization

The ZFC and FC magnetic susceptibility (χ) as a function of T for all samples were measured at 1000 Oe. The FC curves for $Ba_{1+x}La_{1-x}MnSbO_6$ ($0.1 \leq x \leq 0.7$) are shown in Fig. 7a. The susceptibility exhibits a steady rise below ≈200 K for the samples with lower x values showing a ferromagnetic behaviour. At low temperatures, the curves display a cusp between 14 and 21 K depending on the sample. The magnetization shows significant differences between the FC and ZFC data as shown in Fig. 7b for $x = 0.2$, 0.4 and 0.7; and this is due to magnetic frustration in the system which is more remarkable for $x = 0.2$. It is noticeable that χ decreases with increasing x, but in spite of that, the macroscopic ferromagnetic behaviour still remains even for $x = 0.5$ and is not observed at all for $x = 0.6$ and 0.7. The χ^{-1} data for $x = 0.2$ and $x = 0.7$ for FC curves are shown in Fig. 7c. The linear behaviour is more evident for samples with large values of x, for example $x = 0.7$ shown in Fig. 7c and it is consistent with χ vs T measurements that shows no macroscopically observable ferromagnetic behaviour. The high temperature paramagnetic regions ≈ $T > 250$ K were fitted with a Curie-Weiss (CW) law and positive Weiss constants (θ_W) were obtained for all samples, which indicate predominant ferromagnetic correlations in the system. The effective paramagnetic moments experimentally obtained are close to the theoretical ones assuming the calculated ratio of Mn^{2+}/Mn^{3+} for all samples and they were obtained from $\mu^2_{efftheo} = m^*[\mu_{efftheo}(Mn^{2+})]^2 + n^*[\mu_{efftheo}(Mn^{3+})]^2$; where *m* and *n* are stoichiometric coefficients of the corresponding magnetic cations, and $\mu_{efftheo} = g\,(J\,(J+1))^{1/2}$ with $g = 2$. Only spin contribution ($J = S$) to the theoretical magnetic moments are expected for Mn. Table 5 shows the magnetic parameters from Curie-Weiss law fitting of FC data.

The minimum of first derivative dM/dT was used as a criterion to obtain the ferromagnetic transition temperatures (T_C). The T_C were found between ≈150 and 180 K with a small increment compared to $BaLaMnSbO_6$ ($T_C \approx 160$ K) [22] for $0.2 \leq x \leq 0.5$, and this transition temperature could not be established for $x = 0.6$ and $x = 0.7$.

Some double perovskites containing Mn^{2+} have been reported before. Recently, two double perovskites, Mn_3ReO_6 and $MnNbMnSbO_6$, with Mn^{2+} in both A and B sites were informed [46,47]. Similarities with our compounds were found for $SrLaMnSbO_6$ [48]. Positive Weiss constant was observed ($\theta_W = 62$ K) and the effective paramagnetic moment was found to be 5.70 μ_B, which is slightly lower than the calculated one assuming spin only Mn^{2+} in high spin. Their PND data did not show long-range magnetically ordered state above 3.7 K, unlike our case where LRO was found under ≈ 18 K for all samples, being more noticeable for $0.1 \leq x \leq 0.5$.

In our previous publication [22] we show that $BaLaMnSbO_6$ displays signs of SPM in the 40–160 K range, which arises from unbalanced antiferromagnetism inside 3D-nanoclusters formed by regions rich in Mn^{2+}–O^{2-}–Mn^{2+} superexchange paths. In $Ba_{1+x}La_{1-x}MnSbO_6$ the larger the cationic disorder degree, the more frequent the presence of these 3D-nanoclusters. As x gradually rises, the paths in these clusters are transforming into $Mn^{2+/3+}$–O–$Mn^{2+/3+}$, which does not have the same behaviour than the clusters with Mn^{2+}-O-Mn^{2+} paths, since the SPM disappeared (see Fig. 7a).

As stated previously, Mn^{3+} ions preferably occupy the site containing mainly Sb^{5+}. This may be seen in the ⟨B′-O⟩ distances because this average octahedral distance increases slightly with the growth in x and it is due to the incorporation of Mn^{3+} at the Sb^{5+} site. Also, the ASD is more evident when x increases (see occupation values of sites Mn/Sb (1) and Mn/Sb (2) in Table 2) and this is due to the decrease in charge difference between B and B′ sites, which likely also indicates that Mn^{3+} is beginning to accommodate at the site that contains mainly Sb^{5+}.

Moreover, Table 5 shows that θ_W values are lower than the

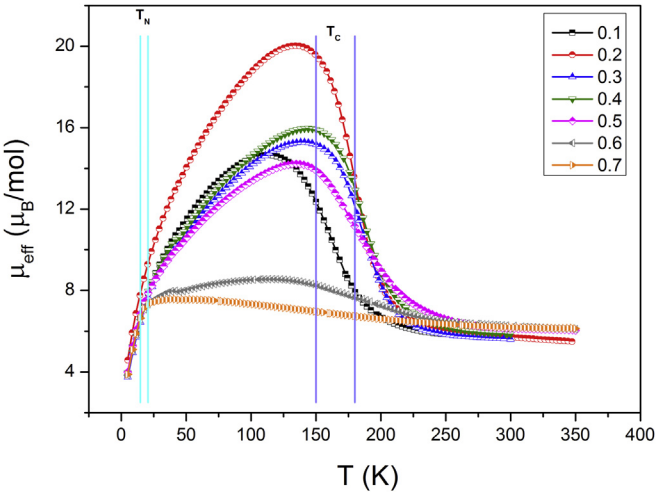

Fig. 8. Thermal evolution of the μ_{eff} obtained from $\chi_m(T)$ vs T data. Straight lines correspond to overall range of T_N (light blue) and T_C (purple). (For interpretation of the references to colour in this figure legend, the reader is referred to the web version of this article.)

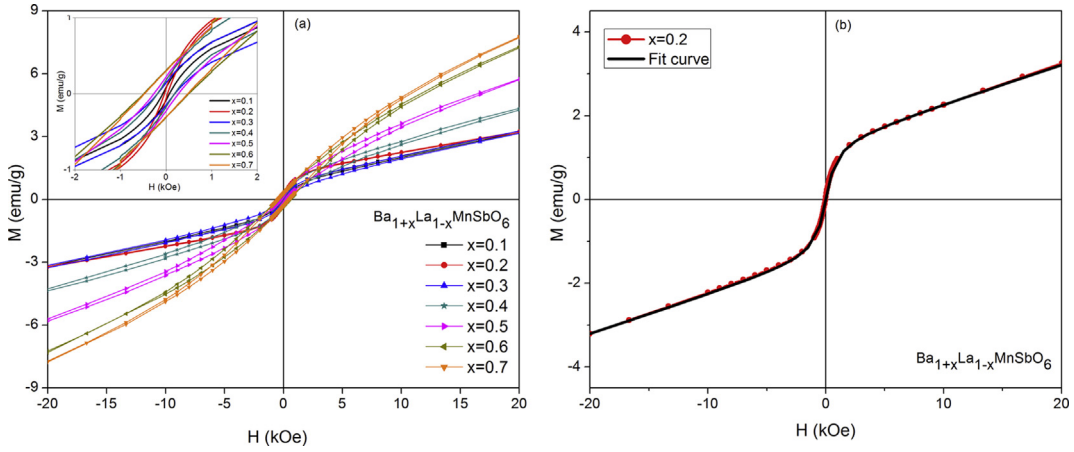

Fig. 9. a) M vs H hysteresis curve at 5 K for $Ba_{1+x}La_{1-x}MnSbO_6$ for $0.1 \leq x \leq 0.7$. Inset: Zoom view for hysteresis curves between −2 and 2 KOe for all samples; **b)** Fitting with Ferromagnetic and Superparamagnetic component for x = 0.2, where red color corresponds to fitting functions.

corresponding T_C values for all samples, which may be related to the competitions of different magnetic interactions in the system or to magnetic frustration.

The thermal evolution of the effective magnetic moment for $Ba_{1+x}La_{1-x}MnSbO_6$ per unit formula is illustrated in Fig. 8 with straight lines indicating the overall range of T_N and T_C. This figure allows to appreciate the differences in the magnetic behaviour as x increases and it can support the superparamagnetic characteristics of these double perovskites that show a maximum for compositions $0.1 \leq x \leq 0.5$ and is not observed for x = 0.6 and 0.7.

Fig. 9a shows the magnetization versus magnetic field (M–H) curves for $Ba_{1+x}La_{1-x}MnSbO_6$ ($0.1 \leq x \leq 0.7$) measured at 5 K. At 300 K a paramagnetic behaviour is observed (linear shape) not showed for simplicity. The magnetic nonlinear behaviour at low temperature and the S-shape of the hysteresis loop are also indications of the presence of superparamagnetic behaviour, which comes from 3D-nanoclusters given by ASD and a weak ferromagnetism that is displayed in the magnetic cells due to canting of spins. The inset of Fig. 9a shows a zoom of the hysteresis loops for all samples.

We perform the fitting of the M vs H curves with excellent agreement using a combination of a ferromagnetic component (weak ferromagnetism), Langevin function for a superparamagnetic contribution and a linear component, as follows:

$$M(H) = \left[\left[A\left[\coth\left(\frac{dH}{T}\right) - \left(\frac{dH}{T}\right)^{-1}\right]\right] + \left[\frac{2M_F}{\pi}\tan^{-1}\left[\frac{\left(H_-^+ H_C\right)}{H_C}\tan\left(\frac{\pi S}{2}\right)\right]\right] + \left[\frac{eH}{T}\right]\right]$$

The first term in brackets corresponds to the Langevin function which describes the SPM behaviour that is usually found in non-interacting magnetic clusters or small particles systems [49]; the second term in brackets corresponds to the ferromagnetic component (WFM), and the last term corresponds to a paramagnetic (PM) contribution and/or a AFM contribution of the entire matrix of the material. The *A* parameter is the maximum saturation achieved by the nanoclusters when these are aligned with a high magnetic field. The *d* parameter is associated with the total magnetic moment for each cluster ($d = \mu_{eff}/K_B$) and *e* is related to the fraction of PM cations and/or macroscopic AFM. M_F corresponds to saturation magnetization of the weak ferromagnetic component, and S is the ratio of M_r/M_F. Where M_r is the remnant magnetization and H_C is the intrinsic coercivity. The parameters obtained from the fitting process are shown in Table 6. The fitting for x = 0.2 is illustrated in Fig. 9b where the black curve is the calculated one. The 3D-nanoclusters even magnetically ordered below T_C are not enough to display a long range magnetic order in PND data at low temperatures because they are not ordered periodically in space; this is the reason for not seen any long range magnetic order until the temperature is below T_N.

The percentage of the total Mn that is included in 3D-nanoclusters rises with x as ASD is becoming larger. However, the size of the 3D-nanoclusters decreases as x increases. As a consequence, with increasing x, there are more 3D-nanoclusters but they are becoming smaller. Consequently, when the 3D-nanoclusters are very small, the magnetic order inside the nanocluster cannot be sustained (samples with x = 0.6 and 0.7) and SPM disappears (Fig. 7a and b). On the other hand, H_c and M_r have a tendency to increase, with an increment of x values shown in Table 6. This ferromagnetic component should be associated with the weak ferromagnetism produced by the canting of the spins of the AFM

Table 6
Magnetic parameters obtained from Langevin, Ferromagnetic and linear functions fitting.

x	Langevin parameters				FM parameters			
	A (μ_B/mol)	Average Mn per clusters	μ_{eff} per cluster (μ_B)	% Mn in 3D-nanoclusters	M_F (μ_B/mol)	% FM	Hc (Oe)	Mr (μ_B/mol)
0.1	0.06	7.00	33.00	1.22	0.05	1.00	76.00	0.01
0.2	0.10	27.00	128.00	2.19	0.03	1.00	36.37	0.01
0.3	0.06	4.00	17.00	1.30	0.06	1.24	191.25	0.01
0.4	0.07	4.00	16.00	1.54	0.07	1.57	189.20	0.02
0.5	0.36	2.00	9.30	8.00	0.08	1.73	275.00	0.02
0.6	0.73	2.00	7.44	17.00	0.10	2.32	500.00	0.03
0.7	0.89	2.00	7.29	20.71	0.10	2.28	483.00	0.03

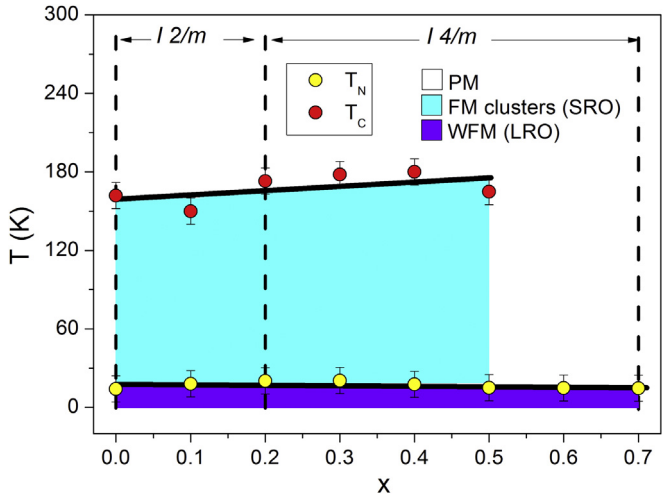

Fig. 10. Magnetic phase diagram for $Ba_{1+x}La_{1-x}MnSbO_6$ with $0.1 \leq x \leq 0.7$.

matrix (see below), which is a little more remarkable in Fig. 9a for $x = 0.6$ and 0.7 because the SPM component has vanished.

From the good refinements of magnetic cell from PND data, we found two coupled antiferromagnetic sublattices with canting, that leads a weak ferromagnetic behaviour below T_N in all samples. This is in good agreement with the irreversibility between ZFC and FC curves shown just for some samples in Fig. 7b which indicates the presence of a weak ferromagnetic behaviour as stated before. Another important fact is the presence of the hysteresis loops at 5 K shown in Fig. 9 for all samples, which further support the presence of a weak ferromagnetism. It is important to mention that undoped $BaLaMnSbO_6$ shows no hysteresis loop and therefore does not show signs of weak ferromagnetism [22]. Also, it is important to remark that we could make the refinement of low temperature PND data with two different magnetic sublattices, which implies the possibility of different antiferromagnetic arrangements, and in our case with the presence of Mn^{3+}, we achieved a frustrated antiferromagnetic arrangement which generates some remanent magnetic moment and gives rise to the weak ferromagnetic behaviour. So, the results of weak ferromagnetic behaviour displayed in PND at low temperature and the presence of SPM 3D-nanoclusters may be the cause of the interesting magnetic properties found for these compounds.

The magnetic phase diagram that resumes the magnetic behaviour of this series of perovskites is shown in Fig. 10, where we can see the coexistence between different magnetic phases. There is a paramagnetic zone, a weak ferromagnetic (WFM) region given by the magnetic LRO, and the superparamagnetic region given by 3D-nanoclusters generating a magnetic short range order for all samples with the exception of $x = 0.6$ and 0.7 where no SPM is evident.

4. Conclusions

$Ba_{1+x}La_{1-x}MnSbO_6$ double perovskites with $0.1 \leq x \leq 0.7$ were synthesized by solid state method in air. X-ray and PND data show that the samples with $x \leq 0.2$ crystallize in the monoclinic space group I 2/m, while the samples with $0.3 \leq x \leq 0.7$ crystallize in the tetragonal space group I 4/m. The volume has noticeable non monotonic variation as x changes, with an increment for $0.1 \leq x \leq 0.2$ and $0.6 \leq x \leq 0.7$ and it decreases for $0.3 \leq x \leq 0.5$, due to a competition between the doping with a bigger <A> cation, which drives the expansion of the volume, and the increase in oxidation from Mn^{2+} to Mn^{3+}, which produces a reduction in volume. The double perovskites were obtained with a high order degree in B and B′ cations that slightly diminishes with Ba doping.

The effective existence of Mn^{2+}/Mn^{3+} mixed valence has been well established by XES measurements, showing an increment of the Mn oxidation state with increasing x values. ASD was found by Rietveld analysis of PND data. This ASD conducted to the existence of 3D-nanoclusters containing $Mn^{2+/3+}$–O–$Mn^{2+/3+}$ superexchange paths. These compounds display signs of SPM in the ≈40–160 K range, which arises from unbalanced antiferromagnetism inside 3D-nanoclusters formed by regions which are rich in $Mn^{2+/3+}$–O–$Mn^{2+/3+}$ paths. The χ vs T curves display a macroscopic ferromagnetic behaviour with Curie temperatures that decrease as doping level increases.

Fitting the M vs H curves with a combination of a linear part, a ferromagnetic component and a Langevin function we were able to figure out that the number of 3D-nanoclusters raised and their size diminished as x increases. This takes into account the behaviour of the χ vs T curves which change from a superparamagnetic behaviour in the 40–160 K range for $0.1 \leq x \leq 0.5$ to a dominant antiferromagnetism for $x = 0.6$ and 0.7.

PND data shows the appearance of new peaks at low angles below ≈20 K indicative of magnetic LRO, which is given by two antiferromagnetic sublattices with a net component of the total magnetic moment that yields a weak ferromagnetic component. This agrees with the maximum observed in the χ vs T curves in this temperature range.

We were able to construct a phase diagram were we localize the different magnetic behaviours as a function of temperature and composition for the series $Ba_{1+x}La_{1-x}MnSbO_6$.

Acknowledgements

Financial support from the Consejo Nacional de Investigaciones Científicas y Técnicas (CONICET) (grant to R. E. C.: PIP #11220120100360, fellowship to D. M. A.), by the Agencia Nacional de Promoción Científica y Tecnológica (grant to R. E. C.: PICT 2013-2149), by the Secretaría de Ciencia y Tecnología de la Universidad Nacional de Córdoba (SECyT-UNC) (project number 203/14). J.A.A. acknowledges the financial support of the Spanish MINECO to the project MAT2013-41099-R. The authors gratefully acknowledge the Institut Laue Langevin (ILL) (Grenoble, France) for access to D2B and D1B powder diffractometers.

Appendix A. Supplementary data

Supplementary data related to this article can be found at http://dx.doi.org/10.1016/j.jallcom.2016.12.308

References

[1] M. DeMarco, H.A. Blackstead, J.D. Dow, M.K. Wu, D.Y. Chen, F.Z. Chien, M. Haka, S. Toorongian, J. Fridmann, Magnetic phase transition in superconducting $Sr_2YRu_{0.95}Cu_{0.05}O_6$ observed by the ^{99}Ru Mössbauer effect, Phys. Rev. B 62 (2000) 14301–14303.
[2] Z. Fang, K. Terakura, J. Kanamori, Strong ferromagnetism and weak antiferromagnetism in double perovskites: Sr_2FeMO_6 (M=Mo, W, and Re), Phys. Rev. B 63 (2001) 180407.
[3] T. Fukushima, A. Stroppa, S. Picozzi, Large ferroelectric polarization in the new double perovskite $NaLaMnWO_6$ induced by non-polar instabilities, Phys. Chem. Chem. Phys. 13 (2011) 12186–12190.
[4] K. Kobayashi, T. Kimura, H. Sawada, K. Terakura, Y. Tokura, Room-temperature magnetoresistance in an oxide material with an ordered double-perovskite structure, Nature 395 (1998) 677–680.
[5] D.D. Sarma, P. Mahadevan, T. Saha-Dasgupta, S. Ray, A. Kumar, Electronic structure of Sr_2FeMoO_6, Phys. Rev. Lett. 85 (2000) 2549–2552.
[6] Y. Shimakawa, M. Azuma, N. Ichikawa, Multiferroic compounds with double-perovskite structures, Materials 4 (2011) 153–168.
[7] D. Serrate, J.M. De Teresa, P.A. Algarabel, C. Marquina, J. Blasco, M.R. Ibarra,

J. Galibert, Magnetoelastic coupling in $Sr_2(Fe_{1-x}Cr_x)ReO_6$ double perovskites, J. Phys. Condens. Matter 19 (2007), 436226 (10pp).
[8] M.T. Anderson, K.B. Greenwood, G.A. Taylor, K.R. Poeppelmeier, B-cation arrangements in double perovskites, Prog. Solid State Chem. 22 (1993) 197–233.
[9] S. Vasala, M. Karppinen, $A_2B'B''O_6$ perovskites: a review, Prog. Solid State Chem. 43 (2015) 1–36.
[10] V.M. Goldschmidt, T. Barth, G. Lunde, W. Zachariasen, Geochemische Verteilungsgesetze der Elemente. VII: Die Gesetze der Krystallochemie vol. 2, 1926, p. 117. Mat. -Nat. Kl.
[11] H.A. Jahn, E. Teller, Stability of polyatomic molecules in degenerate electronic states. I. Orbital degeneracy, Proc. R. Soc. Lond. A 161 (1937) 220–235.
[12] P.M. Woodward, Octahedral tilting in perovskites. I. Geometrical considerations, Acta Crystallogr. Sect. B Struct. Sci. 53 (1997) 32–43.
[13] Qingdi Zhou, B.J. Kennedy, C.J. Howard, M.M. Elcombe, A.J. Studer, Structural phase transitions in $A_{2-x}Sr_xNiWO_6$ (A= Ca or Ba, $0 \leq x \leq 2$) double perovskites, Chem. Mater. 17 (2005).
[14] J.-W.G. Bos, J.P. Attfield, Magnetic frustration in (LaA)$CoNbO_6$ (A=Ca, Sr, and Ba) double perovskites, Phys. Rev. B 70 (2004) 174434(R).
[15] M.C. Viola, M.J. Martínez-Lope, J.A. Alonso, J.L. Martínez, J.M.D. Paoli, S. Pagola, J.C. Pedregosa, M.T. Fernández-Díaz, R.E. Carbonio, Structure and magnetic properties of Sr_2CoWO_6: an ordered double perovskite containing Co^{2+}(HS) with unquenched orbital magnetic moment, Chem. Mater. 15 (2003) 1655–1663.
[16] T. Yang, T. Perkisas, J. Hadermann, M. Croft, A. Ignatov, M. Greenblatt, B-site ordered perovskite $LaSrMnNbO_6$: synthesis, structure and antiferromagnetism, J. Solid State Chem. 183 (2010) 2689–2694.
[17] Q.-h. Li, N. Li, J.-z. Hu, Q. Han, Q.-s. Ma, L. Ge, B. Xiao, M.-x. Xu, The effect of Ca-substitution in La-site on the magnetic properties of La_2CoMnO_6, J. Appl. Phys. 116 (2014) 033905.
[18] Q. Lin, M. Greenblatt, M. Croft, Evolution of structure and magnetic properties in electron-doped double perovskites, $Sr_{2-x}La_xMnWO_6$ ($0 \leq x \leq 1$), J. Solid State Chem. 178 (2005) 1356–1366.
[19] G. Popov, M. Greenblatt, M. Croft, Large effects of A-site average cation size on the properties of the double perovskites $Ba_{2-x}Sr_xMnReO_6$: a d^5-d^1 system, Phys. Rev. B 67 (2003) 024406.
[20] M. Yuste, J.C. Pérez, J. Romero, M.T. Azcondo, F. García, U. Amador, New perovskite materials of the $La_{2-x}Sr_xCoTiO_6$ series, Dalton Trans. 40 (2011) 7908–7915.
[21] M.T. Haque, H. Satoh, N. Kamegashira, Structure and magnetic properties of $Ca_xLa_{2-x}MnIrO_6$ solid solution, J. Alloys Compd. 408 (2006) 1205–1209.
[22] M.C. Blanco, J.M.D. Paoli, S. Ceppi, G. Tirao, V.M. Nassif, J. Guimpel, R.E. Carbonio, Synthesis, structural characterization and magnetic properties of the monoclinic ordered double perovskites BaLaMSbO$_6$, with M = Mn, Co and Ni, J. Alloys Compd. 606 (2014) 139–148.
[23] Chandrahas Bharti, A. Sen, Sadhan Chanda, T.P. Sinha, Structural, vibrational and electrical properties of ordered double perovskite oxide $BaLaMnSbO_6$, J. Alloys Compd. 590 (2014) 125–130.
[24] R.E. Carbonio, D.M. Arciniegas, G.J. Cuello, V. Nassif, Crystal and Magnetic Structure of the New Double Perovskites $Ba_{1+x}La_{1-x}MnSbO_6$ with $0.1<x<0.7$ Containing Mn^{2+}/Mn^{3+} Mixtures, Institut Laue-Langevin (ILL), 2015.
[25] B. Grenier, J.V. Ahlburg, L. Chapon, C. Colin, E. Constable, J.I.D. Silva, Q. Faure, S. Holm, O. Ivashko, M. Kure, B. Lebert, D. Louis, L. Mazzuca, A. Mistonov, J. Muro, B. Ouladdiaf, A. Parabas, P. Parisiadis, D. Pincini, R. Procter, S. Raymond, L.A. Rodríguez, M. Rossi, A. Sapozhnik, S. Sofronova, S.M. Souliou, M. Valiska, J. Vijayakumar, P. Villar, HSC18 Practicals, Institut Laue-Langevin (ILL), 2015.
[26] H.M. Rietveld, A Profile refinement method for nuclear and magnetic structures, J. Appl. Crystallogr. 2 (1969) 65–71.
[27] J. Rodríguez-Carvajal, Recent advances in magnetic structure determination by neutron powder diffraction, Phys. B Condens. Matter 192 (1993) 55–69.
[28] G. Tirao, G. Stutz, C. Cusatis, An inelastic X-ray scattering spectrometer at LNLS, J. Synchrotron Rad. 11 (2004) 335–342.
[29] G. Tirao, S. Ceppi, A.L. Cappelletti, E.V.P. Miner, Oxidation state characterization in Cr oxides by means of Cr-Kβ emission spectroscopy, J. Phys. Chem. Solids 71 (2010) 199–205.
[30] J.A. Bearden, X-Ray wavelengths, Rev. Mod. Phys. 39 (1967) 78–124.
[31] S.P. Limandri, A.C. Carreras, R.D. Bonetto, J.C. Trincavelli, Kβ satellite and forbidden transitions in elements with $12 \leq Z \leq 30$ induced by electron impact, Phys. Rev. A 81 (2010) 012504.
[32] S.S. Raju, B.S. Reddy, M.V.R. Murti, L. Mombasawala, A study of K x-ray hypersatellites and KMM radiative Auger effect (RAE) of the elements $19 \leq Z \leq 25$ by photon excitation, X-ray Spectrom. 36 (2007) 35–41.
[33] S. Ceppi, A. Mesquita, F. Pomiro, E.V.P. Miner, G. Tirao, Study of Kβ X-ray emission spectroscopy applied to $Mn_{(2-x)}V_{(1+x)}O_4$ (x=0 and 1/3) oxyspinel and comparison with XANES, J. Phys. Chem. Solids 75 (2014) 366–373.
[34] J.A. Bearden, A.F. Burr, Reevaluation of X-ray atomic energy levels, Rev. Mod. Phys. 39 (1967) 125–142.
[35] P. Glatzel, U. Bergmann, High resolution 1s core hole X-ray spectroscopy in 3d transition metal complexes—electronic and structural information, Coord. Chem. Rev. 249 (2005) 65–95.
[36] G. Peng, F.M.F. deGroot, K. Haemaelaeinen, J.A. Moore, X. Wang, M.M. Grush, J.B. Hastings, D.P. Siddons, W.H. Armstrong, High-resolution manganese x-ray fluorescence spectroscopy. Oxidation-state and spin-state sensitivity, J. Am. Chem. Soc. 116 (1994) 2914–2920.
[37] E. Cengiz, Z. Bıyıklıoğlu, N. KüpAylıkcı, V. Aylıkcı, G. Apaydın, E. Tıraşoğlu, H. Kantekin, Chemical Effect on K Shell X-ray fluorescence parameters and radiative Auger ratios of Co, Ni, Cu, and Zn complexes, Chin. J. Chem. Phys. 23 (2010) 138–144.
[38] N. Narayanan, D. Mikhailova, A. Senyshyn, D.M. Trots, R. Laskowski, P. Blaha, K. Schwarz, H. Fuess, H. Ehrenberg, Temperature and composition dependence of crystal structures and magnetic and electronic properties of the double perovskites $La_{2-x}Sr_xCoIrO_6$ ($0 \leq x \leq 2$), Phys. Rev. B 82 (2010) 024403.
[39] J. Dawidowski, J.R. Granada, J.R. Santisteban, F. Cantargi, L.A. Rodríguez, in: F. Fernández-Alonso, D.L. Price (Eds.), Appendix: Neutron Scattering Lengths and Cross Sections, vol. 44, Neutron Scattering - Fundamentals Academic Press, 2013, pp. 471–529.
[40] G.Ch. Kostogloudis, N. Vasilakos, Ch. Ftikos, Preparation and characterization of $Pr_{1-x}Sr_xMnO_3 \pm \delta$ (x = 0, 0.15, 0.3, 0.4, 0.5) as a potential SOFC cathode material operating at intermediate temperatures (500–700 °C), J. Eur. Ceram. Soc. 17 (1997) 1513–1521.
[41] R.D. Shannon, Revised effective ionic radii and systematic studies of interatomic distances in halides and chalcogenides, Acta Crystallogr. A 32 (1976) 751–767.
[42] N. Aylikci, E. Tiraşoğlu, I. Karahan, V. Aylikci, E. Cengiz, G. Apaydin, Alloying effect on K shell X-ray fluorescence parameters and radiative Auger ratios of Co and Zn in Zn_xCo_{1-x} alloys, Chem. Phys. Lett. 484 (2010) 368–373.
[43] M.A. Beckwith, M. Roemelt, M. Collomb, C. DuBoc, T. Weng, U. Bergmann, P. Glatzel, F. Neese, S. DeBeer, Manganese Kβ X-ray emission spectroscopy as a probe of metal–ligand interactions, Inorg. Chem. 50 (2011) 8397–8409.
[44] E. Gallo, F. Bonino, J.C. Swarbrick, T. Petrenko, A. Piovano, S. Bordiga, D. Gianolio, E. Groppo, F. Neese, C. Lamberti, P. Glatzel, Preference towards five-coordination in Ti silicalite-1 upon molecular adsorption, Chem. Phys. Chem. 14 (2013) 79–83.
[45] S. Limandri, S. Ceppi, G. Tirao, G. Stutz, C.G. Sánchez, J.A. Riveros, High resolution study of Kβ′ and $Kβ_{1,3}$ X-ray emission lines from Mn-compounds, Chem. Phys. Chem. 367 (2010) 93–98.
[46] A.M. Arévalo-López, F. Stegemann, J.P. Attfield, Competing antiferromagnetic orders in the double perovskite Mn_2MnReO_6 (Mn_3ReO_6), Chem. Commun. 52 (2016) 5558–5560.
[47] E. Solana-Madruga, A.M. Arévalo-López, A.J. Dos Santos-García, E. Urones-Garrote, D. Ávila-Brande, R. Sáez-Puche, J.P. Attfield, Double double cation order in the high-pressure perovskites $MnRMnSbO_6$, Angew. Chem. Int. Ed. 55 (2016) 9340–9344.
[48] T.K. Mandal, A.M. Abakumov, M.V. Lobanov, M. Croft, V.V. Poltavets, M. Greenblatt, Synthesis, structure, and magnetic properties of $SrLaMnSbO_6$: a new B-site ordered double perovskite, Chem. Mater. 20 (2008) 4653–4660.
[49] K. Hayashi, K. Ono, H. Suzuki, M. Sawada, M. Moriya, W. Sakamoto, T. Yogo, One-pot biofunctionalization of magnetic nanoparticles via thiol-ene click reaction for magnetichyperthermia and magnetic resonance imaging, Chem. Mater. 22 (2010) 3768–3772.